

PAPER • OPEN ACCESS

Analytical model of the readout power and SQUID hysteresis parameter dependence of the resonator characteristics of microwave SQUID multiplexers

To cite this article: M Wegner *et al* 2022 *Supercond. Sci. Technol.* **35** 075011

View the [article online](#) for updates and enhancements.

You may also like

- [Macroscopic resonant tunneling in an rf-SQUID flux qubit under a single-cycle sinusoidal driving](#)

Jianxin Shi, , Weiwei Xu et al.

- [Investigation on readout coil design for fluxed locked loop control of HTS rf-SQUID](#)

Y Miyato and H Itozaki

- [Effective Hamiltonians for interacting superconducting qubits: local basis reduction and the Schrieffer–Wolff transformation](#)

Gioele Consani and Paul A Warburton



IOP | ebooks™

Bringing together innovative digital publishing with leading authors from the global scientific community.

Start exploring the collection—download the first chapter of every title for free.

Analytical model of the readout power and SQUID hysteresis parameter dependence of the resonator characteristics of microwave SQUID multiplexers

M Wegner^{1,2,3,*} , C Enss^{1,3} and S Kempf^{1,2,3} 

¹ Kirchhoff-Institute for Physics, Heidelberg University, Im Neuenheimer Feld 227, D-69120 Heidelberg, Germany

² Institute of Micro- and Nanoelectronic Systems, Karlsruhe Institute of Technology, Hertzstrasse 16, Building 06.41, D-76187 Karlsruhe, Germany

³ Institute for Data Processing and Electronics, Karlsruhe Institute of Technology, Hermann-von-Helmholtz-Platz 1, Building 242, D-76344 Eggenstein-Leopoldshafen, Germany

E-mail: mathias.wegner@kit.edu

Received 15 December 2021, revised 2 May 2022

Accepted for publication 5 May 2022

Published 6 June 2022



Abstract

We report on the development of an analytical model describing the readout power and superconducting quantum interference device (SQUID) hysteresis parameter dependence of the resonator characteristics used for frequency encoding in microwave SQUID multiplexers. Within the context of this model, we derived the different dependencies by analyzing the Fourier components of the non-linear response of the non-hysteretic rf-SQUID. We show that our model contains the existing model as a limiting case, leading to identical analytical expressions for small readout powers. Considering the approximations we made, our model is valid for rf-SQUID hysteresis parameters $\beta_L < 0.6$ which fully covers the parameter range of existing multiplexer devices. We conclude our work with an experimental verification of the model. In particular, we demonstrate a very good agreement between measured multiplexer characteristics and predictions based on our model.

Keywords: microwave SQUID multiplexer, non-linear Josephson inductance, Josephson junction, non-hysteretic rf-SQUID, cryogenic detector array readout, superconducting microwave resonators

(Some figures may appear in colour only in the online journal)

* Author to whom any correspondence should be addressed.



Original Content from this work may be used under the terms of the [Creative Commons Attribution 4.0 licence](https://creativecommons.org/licenses/by/4.0/). Any further distribution of this work must maintain attribution to the author(s) and the title of the work, journal citation and DOI.

1. Introduction

Superconducting quantum interference devices (SQUIDs) are the devices of choice for measuring any physical quantity that can be naturally converted into a magnetic flux change. They provide noise levels close to the quantum limit as well as ultra-low power dissipation down to a few pW for single devices [1, 2]. SQUIDs are hence intrinsically compatible with sub-Kelvin operation temperatures and are thus particularly suited for reading out cryogenic particle detectors, such as transition edge sensors (TESs) [3] or magnetic microcalorimeters (MMCs) [4]. Both, TESs and MMCs, are calorimetric single-particle detectors converting an energy input upon the absorption of an energetic particle into a temperature rise that is continuously monitored via an ultra-sensitive thermometer that is based either on the steep temperature dependence of the resistance within the S/N transition of a superconducting material (TESs) or the temperature dependence of a paramagnetic material that is situated in a weak external bias magnetic field. The unique combination of such ultra-sensitive thermometers and a SQUID-based readout chain ultimately yields energy-dispersive single-particle detectors with outstanding energy resolution, fast signal rise time, a quantum efficiency close to 100% and a large dynamic range.

The maturity of fabrication technologies allows building large-scale detector systems employing thousands or even millions of virtually identical detectors paving the way for realizing next-generation instruments such as the Simons observatory [5] or experiments investigating the electron neutrino mass [6, 7] with sub-eV/ c^2 mass sensitivity. However, for this kind of instruments, system complexity, cooling power at the cryogenic platform as well as overall costs have to be taken into account. For these reasons, SQUID based multiplexing techniques turn out to be key technologies for these applications.

Existing SQUID-based cryogenic multiplexers rely on time-division multiplexing [8], frequency-division multiplexing using MHz [9] and GHz [10] carriers, code-division multiplexing [11] using orthogonal Walsh codes or hybrid techniques [12]. Among these techniques, microwave SQUID multiplexing (μ MUXing) [13] is thought to be best suited for realizing ultra-large scale detector arrays since this technique offers a large multiplexing factor, the required bandwidth per readout channel for fast calorimetric detectors, a very good noise performance as well as an extremely low on-chip power dissipation. However, realizing and in particular optimizing such complex readout systems requires detailed models describing the device physics to reliably predict the performance of the readout system on the basis of design and operation parameters.

The existing model leads to an accurate description of the μ MUX characteristics for small readout powers, i.e. $P_{\text{rf}} \rightarrow 0$ [14, 15]. For experimentally more realistic values, i.e., when using a μ MUX for cryogenic detector readout, large discrepancies between measurements and model predictions are observed [15]. For this reason, the existing μ MUX model cannot reliably be used for optimizing the device

performance. However, operating the cryogenic multiplexer with optimal parameters is of utmost importance as its performance influences the overall system noise level and potentially might limit the achievable energy resolution [4].

Against this background, we present a μ MUX model that precisely allows predicting the characteristics of a μ MUX for a wide parameter range of the readout signal amplitude and the SQUID hysteresis parameter. We compare our model with the existing model reliably predicting the μ MUX performance for small readout powers to determine parameter constraints and show that our model includes existing models as a limiting case. We conclude our work with an experimental verification of our model. Here, we demonstrate an excellent agreement between predictions based on our model and measured μ MUX characteristic curves.

2. Basics of microwave SQUID multiplexing

To allow for a direct comparison between the existing model and the model described in this publication and to introduce the nomenclature that we use in the following, we summarize the basic theoretical concepts of microwave SQUID multiplexing in this section. A more detailed description of the model can be found, for example, in [14, 15].

Figure 1 shows the schematic circuit diagram of a single μ MUX readout channel. It consists of a coplanar, quarter-wave resonator with characteristic impedance Z_0 and physical length l_r . The resonance frequency of the unloaded resonator is

$$f_0 = \frac{1}{4l_r \sqrt{(L'_m + L'_{\text{kin}}) C'}}, \quad (1)$$

where L'_m , L'_{kin} and C' denote the geometrical (magnetic) inductance, the kinetic inductance of the Cooper pairs and the geometrical (electric) capacitance per unit length, respectively. The open end of the resonator is coupled to a microwave transmission line with characteristic impedance Z_0 via a coupling capacitor with capacitance C_c . The other end of the resonator is shorted to ground via a load inductor with inductance L_T that is simultaneously used to weakly couple a non-hysteretic rf-SQUID to the resonator. The rf-SQUID consists of a superconducting loop with inductance L_S which is interrupted by a single Josephson tunnel junction with critical current I_c . To guarantee for a non-hysteretic behavior, the SQUID hysteresis parameter $\beta_L = 2\pi L_S I_c / \Phi_0$ is set to $\beta_L \leq 1$. Here, $\Phi_0 = 2.07 \times 10^{-15}$ Vs denotes the magnetic flux quantum. The coupling strength between resonator and rf-SQUID is quantified by the mutual inductance M_T .

For a vanishing coupling strength between resonator and rf-SQUID, i.e. $M_T \rightarrow 0$, the input impedance of the loaded resonator is given by the series connection of the coupling capacitance and the terminated resonator:

$$Z_{\text{in}} = \frac{1}{i\omega C_c} + Z_0 \frac{i\omega L_T + Z_0 \tanh(\gamma l_r)}{Z_0 + i\omega L_T \tanh(\gamma l_r)}. \quad (2)$$

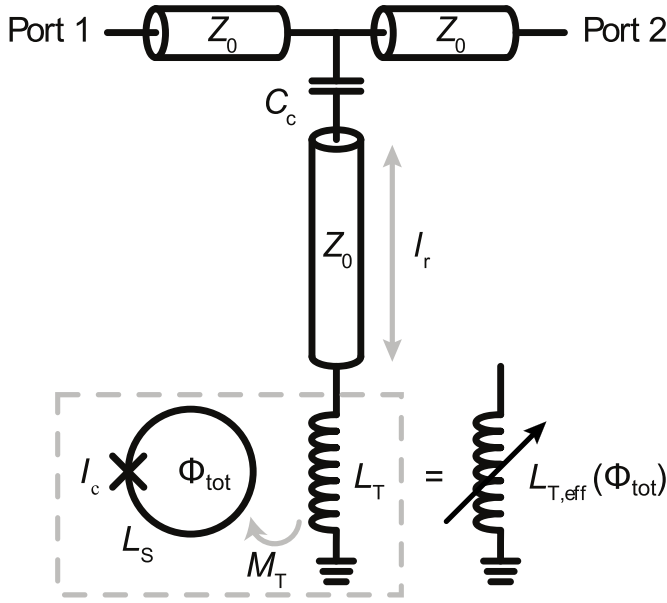


Figure 1. Schematic circuit diagram of a single μ MUX readout channel. The two main components are (i) a non-hysteretic rf-SQUID consisting of a closed superconducting loop with loop inductance L_S and a Josephson tunnel junction with critical current I_c and (ii) a coplanar, quarter-wave resonator with geometrical length l_r that is coupled to a microwave transmission line via a coupling capacitor C_c and shorted to ground via a load inductor L_T . The effective load inductance $L_{T,\text{eff}}$ takes into account the magnetic field dependence of the load inductor L_T due to the mutual interaction with the rf-SQUID.

Here, γ describes the complex propagation constant of the electromagnetic wave with angular frequency ω inside the resonator. Using the condition $\text{Im}(Z_{\text{in}}) = 0$, we yield the expression

$$f_r \approx \frac{f_0}{1 + 4f_0(C_c Z_0 + L_T/Z_0)} \quad (3)$$

for the resonance frequency of the loaded resonator, which is shifted toward smaller frequencies as compared to the resonance frequency f_0 of the unloaded resonator.

We describe the mutual interaction between the rf-SQUID and the resonator by introducing an effective impedance of the resonator termination. Here, for simplicity, we model the Josephson junction as a pure non-linear inductor with inductance $L_{JJ}(\varphi_{\text{tot}}) = \Phi_0 / [2\pi I_c \cos(\varphi_{\text{tot}})]$, which depends on the normalized total magnetic flux $\varphi_{\text{tot}} = 2\pi\Phi_{\text{tot}}/\Phi_0$ threading the SQUID loop, and hence neglects the subgap resistance R_{sg} and the intrinsic capacitance C_{JJ} , as their contribution is about an order of magnitude smaller for most devices. In this case, the inductance $L_{T,\text{eff}}$ of the effective load inductor is given by the expression

$$L_{T,\text{eff}}(\varphi_{\text{tot}}) = L_T - \frac{M_T^2}{L_S + L_{JJ}(\varphi_{\text{tot}})} = L_T - \frac{M_T^2}{L_S} \frac{\beta_L \cos(\varphi_{\text{tot}})}{1 + \beta_L \cos(\varphi_{\text{tot}})}. \quad (4)$$

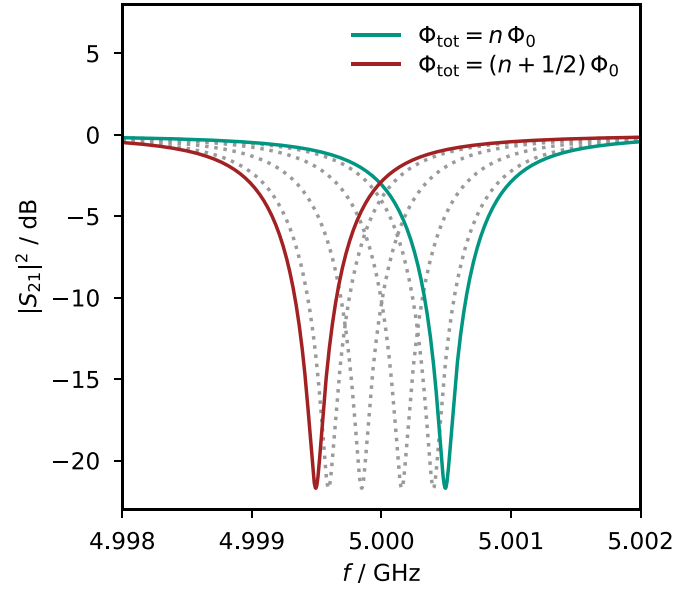


Figure 2. Frequency dependence of the transmission amplitude $|S_{21}(f)|^2$ of a single multiplexer channel for different values of the magnetic flux Φ_{tot} threading the SQUID loop. The colored curves indicate the curves with highest (green line) and lowest (red line) resonance frequency. The parameters used for calculating the curves are $f_r = 5$ GHz, $\Delta f_{\text{BW}} = 1$ MHz, $Z_0 = 50 \Omega$, $M_T^2/L_S = 25.4$ pH and $\beta_L = 0.01$, leading to a maximum resonance frequency shift of $\Delta f_r^{\text{max}} = 1$ MHz. Here, Δf_{BW} describes the resonator bandwidth. The total magnetic flux Φ_{tot} is varied between $n\Phi_0$ and $(n + 1/2)\Phi_0$ in steps of $0.1\Phi_0$.

Using equation (3) and replacing L_T by $L_{T,\text{eff}}(\varphi_{\text{tot}})$ allows deriving an approximation for the magnetic flux dependence of the resonance frequency of the loaded resonator:

$$f_r(\varphi_{\text{tot}}) \approx f_0 - 4f_0^2 \left[C_c Z_0 + \frac{L_T}{Z_0} - \frac{M_T^2}{Z_0 L_S} \frac{\beta_L \cos(\varphi_{\text{tot}})}{1 + \beta_L \cos(\varphi_{\text{tot}})} \right]. \quad (5)$$

Here, we assumed weak capacitive coupling, i.e. $\omega_0 C_c Z_0 \ll 1$ with $\omega_0 = 2\pi f_0$, and small frequency shifts caused by the SQUID, i.e. $\omega_0 L_T \ll Z_0$.

To illustrate the flux dependence of the resonance frequency, figure 2 shows the transmission amplitude $|S_{21}(f)|^2 = |2/(2 + Z_0/Z_{\text{in}}(f))|^2$ between port 1 and port 2 of an exemplary resonator for different values of the magnetic flux Φ_{tot} . As one can see, the resonance frequency oscillates in between its maximum for $\Phi_{\text{tot}} = n\Phi_0$ and its minimum for $\Phi_{\text{tot}} = (n + 1/2)\Phi_0$. For a magnetic flux of $\Phi_{\text{tot}} = (n \pm 1/4)\Phi_0$, the Josephson inductance $L_{JJ}(\varphi_{\text{tot}})$ diverges, and therefore the resonance frequency $f_r((n \pm 1/4)\Phi_0) = 5$ GHz is simply given by equation (3) since the resonance frequency is not affected by means of the rf-SQUID.

In figure 3 the impact of the hysteresis parameter β_L on the flux-dependent resonance frequency shift $f_r(\Phi_{\text{tot}})$ is shown. For very small values of the SQUID hysteresis parameter, i.e. $\beta_L \rightarrow 0$, screening currents and therefore self-induced magnetic flux contributions Φ_{scr} within the SQUID loop are

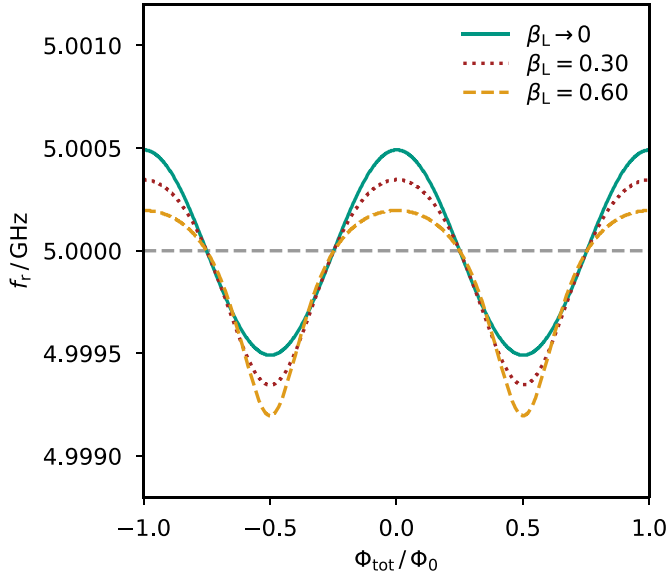


Figure 3. Flux dependence of the resonance frequency $f_r(\Phi_{\text{tot}})$ for different values of the SQUID hysteresis parameter β_L . The ratio M_T^2/L_S is adapted to the corresponding value of β_L in such a way that the maximum resonance frequency shift $\Delta f_r^{\text{max}} = 1$ MHz stays constant. All other parameters of the curves correspond to the values chosen in figure 2.

negligibly small. These characteristics are therefore highly symmetric and describe an ideal sinusoidal behavior around its center frequency. For larger values of β_L , screening currents within the SQUID loop become relevant leading to an asymmetric response and to a general shift of the resonance frequency toward smaller frequencies.

3. Revised model for describing the characteristics of a microwave SQUID multiplexer

The existing μMUX model can be used to accurately determine the μMUX characteristics in the limit of very low readout powers, i.e. $P_{\text{rf}} \rightarrow 0$. However, large deviations between measured characteristics and model predictions are observed for increasingly high readout powers [15]. The μMUX model described in the following is able to describe the effects occurring at high readout powers, thus allowing to describe the μMUX characteristics over the entire practically used readout power range.

3.1. Effective load inductance

An electromagnetic wave with power P_{rf} and angular frequency ω being close to the resonance frequency of the resonator, i.e. $\omega \approx 2\pi f_r$, and traversing from port 1 to port 2 of the microwave transmission line leads to an oscillating current $i_T(t) = I_T \sin(\omega t)$ within the inductance L_T terminating the microwave resonator. On resonance, i.e. for $\omega = 2\pi f_r$, the amplitude of the current reaches the maximum value

$$I_T = \sqrt{\frac{16 Q_1^2 P_{\text{rf}}}{\pi Q_c Z_0}}. \quad (6)$$

Here, Q_1 and Q_c denote the loaded quality factor and the coupling quality factor of the resonator, respectively. Due to the mutual inductance M_T between resonator termination and SQUID loop, the current $i_T(t)$ generates a sinusoidal magnetic flux signal with amplitude $\Phi_{\text{rf}} = M_T I_T$ in the rf-SQUID. Considering an additional, external quasi-static magnetic flux contribution Φ_{ext} as induced by a signal source to be measured, e.g. caused by an inductively coupled input coil, the current in the rf-SQUID can be expressed as

$$I_S(t) = -I_c \sin \left[\varphi_{\text{ext}} + \varphi_{\text{rf}} \sin(\omega t) + \beta_L \frac{I_S(t)}{I_c} \right]. \quad (7)$$

Here, $\varphi_{\text{ext}} = 2\pi \Phi_{\text{ext}}/\Phi_0$ and $\varphi_{\text{rf}} = 2\pi \Phi_{\text{rf}}/\Phi_0$ denote normalized magnetic flux values. The last term in equation (7) is the normalized magnetic flux $\varphi_{\text{scr}}(t) = 2\pi I_S(t) L_S/\Phi_0 = \beta_L I_S(t)/I_c$ that is induced by the supercurrent running in the SQUID loop. The supercurrent $I_S(t)$ inductively couples to the resonator termination, creating a high frequency flux signal $\Phi_T(t) = M_T I_S(t)$ within the termination. Therefore, in accordance to Lenz's law, the voltage $u_{\text{ind}}(t) = -M_T dI_S(t)/dt$ and hence the current

$$i_{\text{ind}}(t) = -\frac{M_T}{i\omega L_T} \frac{dI_S(t)}{dt} \quad (8)$$

are induced in the resonator termination. The total current $i_{\text{tot}}(t) = i_T(t) + i_{\text{ind}}(t)$ in the resonator termination is hence a superposition of two contributions originating from the microwave signal probing the resonator and the supercurrent flowing within the SQUID loop. The total voltage across the resonator termination, $u_{\text{tot}}(t) = L_T di_{\text{tot}}(t)/dt = L_{T,\text{eff}} di_T(t)/dt$, can hence be expressed by introducing an effective inductance

$$L_{T,\text{eff}} = L_T \frac{i_{\text{tot}}(t)}{i_T(t)} = L_T \left(1 + \frac{i_{\text{ind}}(t)}{i_T(t)} \right) \quad (9)$$

of the resonator termination.

3.2. μMUX characteristics for small readout powers, i.e. $P_{\text{rf}} \rightarrow 0$

The characteristics of a μMUX for small readout powers, i.e. $\varphi_{\text{rf}} \rightarrow 0$, can be obtained by calculating the time derivative of equation (7). For this, the function

$$F(I_S, t) = I_S + I_c \sin \left[\varphi_{\text{ext}} + \varphi_{\text{rf}} \sin(\omega t) + \beta_L \frac{I_S}{I_c} \right] = 0 \quad (10)$$

is defined to calculate the implicit derivative

$$\begin{aligned} \frac{dI_S(t)}{dt} &= -\frac{\partial F(I_S, t)/\partial t}{\partial F(I_S, t)/\partial I_S} \\ &= -\frac{I_c \varphi_{\text{rf}} \omega \cos \left[\varphi_{\text{ext}} + \varphi_{\text{rf}} \sin(\omega t) + \beta_L \frac{I_S}{I_c} \right]}{1 + \beta_L \cos \left[\varphi_{\text{ext}} + \varphi_{\text{rf}} \sin(\omega t) + \beta_L \frac{I_S}{I_c} \right]} \cos(\omega t) \\ &\approx -\frac{I_c \varphi_{\text{rf}} \omega \cos(\varphi_{\text{tot}})}{1 + \beta_L \cos(\varphi_{\text{tot}})} \cos(\omega t). \end{aligned} \quad (11)$$

In the last transformation, $\varphi_{rf} \rightarrow 0$ is assumed, yielding $\varphi_{tot} \approx \varphi_{ext} + \beta_L I_S / I_c$. The induced current in the resonator termination can hence be calculated straightforwardly by using equation (8):

$$i_{ind}(t) = -\frac{I_c \varphi_{rf} M_T}{L_T} \frac{\cos(\varphi_{tot})}{1 + \beta_L \cos(\varphi_{tot})} \sin(\omega t). \quad (12)$$

It is phase-shifted by $\pi/2$ due to the complex impedance $i\omega L_T$ of the resonator termination. Combining equations (9) and (12) allows to calculate the effective resonator termination

$$L_{T,eff}(\varphi_{tot}) = L_T - \frac{M_T^2}{L_S} \frac{\beta_L \cos(\varphi_{tot})}{1 + \beta_L \cos(\varphi_{tot})}. \quad (13)$$

This expression is identical to equation (4) derived within the existing μ MUX model.

3.3. μ MUX characteristics for small SQUID hysteresis parameter, i.e. $\beta_L \rightarrow 0$

For a vanishing SQUID hysteresis parameter, i.e. $\beta_L \rightarrow 0$, the flux generated by the supercurrent within the SQUID loop becomes negligible and the third term in equation (7) can be omitted. The supercurrent can then be decomposed into a Fourier series:

$$\begin{aligned} I_S(t) &\approx -I_c \sin(\varphi_{ext} + \varphi_{rf} \sin(\omega t)) \\ &= -I_c \sin(\varphi_{ext}) \cos(\varphi_{rf} \sin(\omega t)) \\ &\quad - I_c \cos(\varphi_{ext}) \sin(\varphi_{rf} \sin(\omega t)) \\ &= -I_c \sin(\varphi_{ext}) \left[J_0(\varphi_{rf}) + 2 \sum_{i=1}^{\infty} J_{2i}(\varphi_{rf}) \cos(2i\omega t) \right] \\ &\quad - I_c \cos(\varphi_{ext}) \left[2 \sum_{i=0}^{\infty} J_{2i+1}(\varphi_{rf}) \sin([2i+1]\omega t) \right], \end{aligned} \quad (14)$$

where $J_i(x)$ denote the Bessel functions of first kind.

The supercurrent $I_S(t)$ and consequently the current $i_{ind}(t)$ in the resonator termination contain Fourier components with multiples of the angular frequency ω . However, due to the resonance condition (see equation (3)), only the fundamental frequency ω populates the resonator. Higher harmonics do not meet the resonance condition and hence interfere destructively within the cavity. Using equations (9) and (12), we yield the induced current

$$i_{ind}(t) = -\frac{2I_c M_T}{L_T} \cos(\varphi_{ext}) J_1(\varphi_{rf}) \sin(\omega t) \quad (15)$$

within the resonator termination and consequently the flux dependence of the resonance frequency:

$$f_r(\varphi_{ext}, \varphi_{rf}) \approx f_0 - 4f_0^2 \left[C_c Z_0 + \frac{L_T}{Z_0} - \frac{M_T^2}{Z_0 L_S} \frac{2\beta_L}{\varphi_{rf}} J_1(\varphi_{rf}) \cos(\varphi_{ext}) \right]. \quad (16)$$

For small SQUID hysteresis parameters, i.e. $\beta_L \rightarrow 0$, and small readout signals, i.e. $\varphi_{rf} \rightarrow 0$, our model and the existing model (see equation (5)) yield identical results since

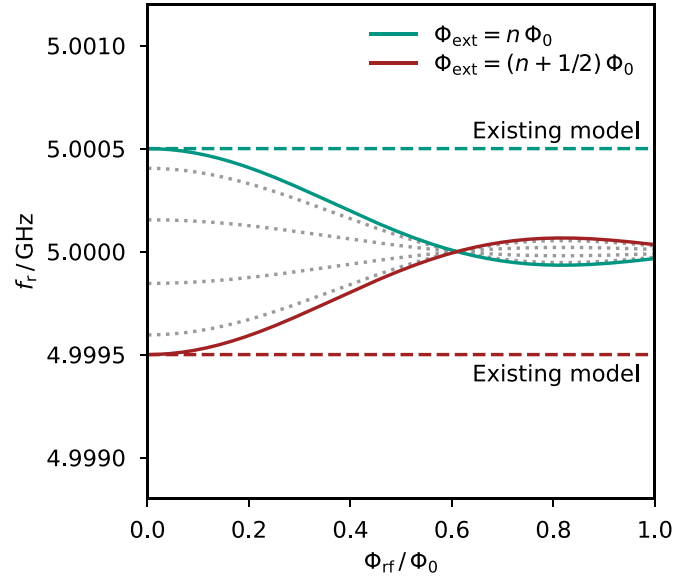


Figure 4. Dependence of the resonance frequency $f_r(\Phi_{rf})$ on the flux amplitude Φ_{rf} of the probe signal for different values of the external flux Φ_{ext} for multiplexer with vanishing SQUID hysteresis parameter, i.e. $\beta_L \rightarrow 0$. The curves are based on equation (16) and their parameters are equal to the parameters chosen in figure 2. The external magnetic flux Φ_{ext} is varied between $n\Phi_0$ and $(n + 1/2)\Phi_0$ in steps of $0.1\Phi_0$. For comparison, the corresponding curves of the existing model are plotted as dashed lines.

$1 + \beta_L \cos(\varphi_{tot}) \rightarrow 1$ and $2J_1(\varphi_{rf})/\varphi_{rf} \rightarrow 1$. However, for probing signals with finite readout power, i.e. $\varphi_{rf} > 0$, the maximum resonance frequency shift Δf_r^{\max} differs from the prediction of the existing μ MUX model as indicated by figure 4. With increasing readout power φ_{rf} , the non-linear response of the Josephson junction converts more and more signal power into higher harmonics that do not match the resonance condition of the resonance circuit. This leads to a decrease in the maximum resonance frequency shift Δf_r^{\max} with increasing readout power. For $\Phi_{rf} \approx 0.61\Phi_0$, we get $J_1(\varphi_{rf}) = 0$ and consequently the resonance frequency $f_r(\Phi_{ext})$ gets independent of the external flux Φ_{ext} . With further increase in readout power, the curves start to oscillate around the center frequency at $f_r(\Phi_{ext} = [n \pm 1/4]\Phi_0)$. The resonance frequencies for $\Phi_{ext} = n\Phi_0$ and $\Phi_{ext} = (n + 1/2)\Phi_0$ might therefore swap their positions depending on the amplitude range of the probe signal.

3.4. μ MUX characteristics for finite hysteresis parameter and probe signal amplitude

Using trigonometric identities, we can rewrite equation (7) as

$$I_S(t) = -I_c \sin \left[\varphi_{ext} + \varphi_{rf} \sin(\omega t) + \beta_L \frac{I_S(t)}{I_c} \right] \quad (17)$$

$$\begin{aligned} &= -I_c \sin(\varphi_{ext} + \varphi_{rf} \sin(\omega t)) \cos \left[\beta_L \frac{I_S(t)}{I_c} \right] \\ &\quad - I_c \cos(\varphi_{ext} + \varphi_{rf} \sin(\omega t)) \sin \left[\beta_L \frac{I_S(t)}{I_c} \right]. \end{aligned} \quad (18)$$

Table 1. Set of parameters used for calculating the resonance frequency $f_r(\varphi_{\text{ext}}, \varphi_{\text{rf}})$ according to equation (20).

	$a_{i,j}$	$b_{i,j}$	$c_{i,j}$		$a_{i,j}$	$b_{i,j}$	$c_{i,j}$
$p_{0,0}$	+1	0	1	$p_{7,2}$	+137/512	7	6
$p_{1,0}$	-1/2	1	2	$p_{7,3}$	-267/1024	7	8
$p_{2,0}$	-1/8	2	1	$p_{8,0}$	+21/1024	8	1
$p_{2,1}$	+3/8	2	3	$p_{8,1}$	-35/512	8	3
$p_{3,0}$	+1/8	3	2	$p_{8,2}$	+103/512	8	5
$p_{3,1}$	-5/16	3	4	$p_{8,3}$	-651/2048	8	7
$p_{4,0}$	+1/16	4	1	$p_{8,4}$	+547/2048	8	9
$p_{4,1}$	-5/32	4	3	$p_{9,0}$	-63/2048	9	2
$p_{4,2}$	+9/32	4	5	$p_{9,1}$	+27/256	9	4
$p_{5,0}$	-5/64	5	2	$p_{9,2}$	-1089/4096	9	6
$p_{5,1}$	+3/16	5	4	$p_{9,3}$	+193/512	9	8
$p_{5,2}$	-17/64	5	6	$p_{9,4}$	-1139/4096	9	10
$p_{6,0}$	-15/512	6	1	$p_{10,0}$	-105/8192	10	1
$p_{6,1}$	+57/512	6	3	$p_{10,1}$	+435/8192	10	3
$p_{6,2}$	-115/512	6	5	$p_{10,2}$	-2595/16384	10	5
$p_{6,3}$	+133/512	6	7	$p_{10,3}$	+5705/16384	10	7
$p_{7,0}$	+21/512	7	2	$p_{10,4}$	-7317/16384	10	9
$p_{7,1}$	-77/512	7	4	$p_{10,5}$	+4807/16384	10	11

Expression (18) can be expanded as a polynomial equation by using a 2nd order Taylor expansion with respect to β_L , i.e. by using the approximations $\cos(\beta_L I_S(t)/I_c) \approx 1 - (\beta_L I_S(t)/I_c)^2/2$ and $\sin(\beta_L I_S(t)/I_c) \approx (\beta_L I_S(t)/I_c)$. Solving the resulting quadratic equation for the supercurrent $I_S(t)$ yields the solutions

$$I_S(\varphi) \approx -I_c \frac{-1 - \beta_L \cos(\varphi) \pm \sqrt{1 + 2\beta_L \cos(\varphi) + \beta_L^2 [1 + \sin(\varphi)^2]}}{\beta_L^2 \sin(\varphi)} \quad (19)$$

with $\varphi = \varphi_{\text{ext}} + \varphi_{\text{rf}} \sin(\omega t)$. Here, the solution with positive sign is relevant as the other solution leads to a divergence for $\sin(\varphi) \rightarrow 0$.

The derivation of the flux-dependent resonance frequency shift is carried out similarly as shown in section 3.3 for a negligibly small hysteresis parameter β_L . However, in contrast to the previous section, a straightforward analytical derivation is not possible due to the complex time dependence of the time derivative of equation (19). To solve the equations, we perform a second Taylor approximation with respect to the parameter β_L . Within the context of this work, a 10th order Taylor expansion was used. However, higher-order terms can in general be included. Similarly to section 3.3, we introduce Bessel functions $J_i(x)$ of first kind and neglect all terms that contain multiples of the angular frequency ω as they do not match the resonance condition. This finally leads to

$$f_r(\varphi_{\text{ext}}, \varphi_{\text{rf}}) \approx f_0 - 4f_0^2 \left[C_c Z_0 + \frac{L_T}{Z_0} - \frac{M_T^2}{Z_0 L_S} \frac{2\beta_L}{\varphi_{\text{rf}}} \sum_{i,j} p_{i,j} \right] \quad (20)$$

with $p_{i,j} = a_{i,j} \beta_L^{b_{i,j}} J_1(c_{i,j} \varphi_{\text{rf}}) \cos(c_{i,j} \varphi_{\text{ext}})$. The parameters $a_{i,j}$, $b_{i,j}$ and $c_{i,j}$ are summarized in table 1. Here, i denotes the

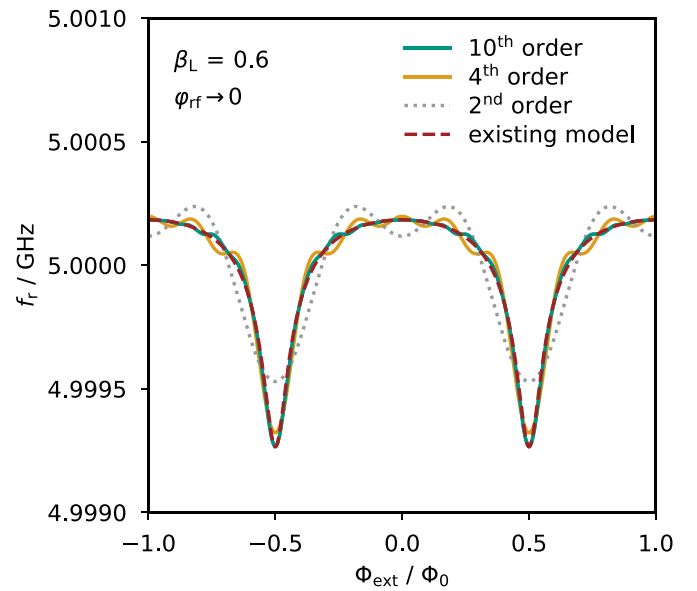


Figure 5. Flux dependence of the resonance frequency $f_r(\Phi_{\text{ext}})$ calculated by means of our μ MUX model for a negligibly small amplitude of the readout signal, i.e. $\varphi_{\text{rf}} \rightarrow 0$, and a SQUID hysteresis parameter of $\beta_L = 0.6$. The ratio M_T^2/L_S is adapted to β_L to achieve $\Delta f_r^{\text{max}} = 1$ MHz, whereas all other parameters equal the parameters chosen in figure 2.

Taylor expansion order and j addresses different contributions of each order.

To estimate the accuracy of our approximation, we show in figure 5 the dependence of the resonance frequency $f_r(\Phi_{\text{ext}})$ on the external flux Φ_{ext} for (i) the existing μ MUX model and an approximation based on (ii) a 2nd order, (iii) a 4th order, and (iv) a 10th order Taylor expansion assuming a SQUID with $\beta_L = 0.6$ and a probing signal with negligible readout power, i.e. $\varphi_{\text{rf}} \rightarrow 0$. The curve obtained by means of the existing model is exact for the chosen parameter range,

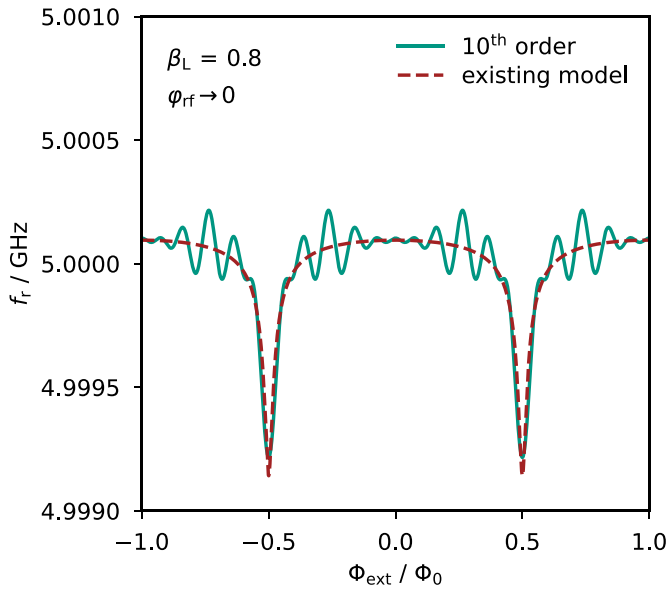


Figure 6. Flux dependence of the resonance frequency $f_r(\Phi_{\text{ext}})$ calculated by means of our μMUX model based on a 10th order Taylor expansion and the existing model for a negligibly small amplitude of the readout signal, i.e. $\varphi_{\text{rf}} \rightarrow 0$, and a SQUID hysteresis parameter of $\beta_L = 0.8$. The ratio M_T^2/L_S is adapted to β_L to achieve $\Delta f_r^{\text{max}} = 1$ MHz, whereas all other parameters equal the parameters chosen in figure 2.

i.e. $\varphi_{\text{rf}} \rightarrow 0$, and essentially equals the corresponding curve shown in figure 3. However, in contrast to figure 3, a transformation $\Phi_{\text{tot}} \rightarrow \Phi_{\text{ext}}$ was applied for allowing a direct comparison between the different models. The plot demonstrates a large deviation between the exact model and approximations based on low-order Taylor expansions and confirms a very good agreement between the existing model and the approximation based on a 10th order Taylor expansion. Therefore, lower-order approximations are only valid for small hysteresis parameters β_L . In the same way, the approximation based on a 10th order Taylor expansion becomes more and more imprecise for $\beta_L > 0.6$. For example, for $\beta_L = 0.8$ the characteristics based on the 10th order model deviate significantly from the exact model (see figure 6). To conclude, these results indicate that our model is valid in the range of $\beta_L \leq 0.6$ and can potentially be fitted to $\beta_L > 0.6$ when using higher-order Taylor expansions. However, for existing μMUX s, the hysteresis parameter is typically $\beta_L < 0.6$, thus our model based on the 10th order Taylor expansion covers the relevant parameter range.

Figure 7 shows the dependence of the resonance frequency $f_r(\Phi_{\text{rf}})$ on the amplitude Φ_{rf} of the probing signal for different values of the external flux Φ_{ext} and the hysteresis parameter β_L as calculated using our model. The characteristics for $\beta_L \rightarrow 0$ describe the limit of vanishing self-induced flux ($\Phi_{\text{scr}} \rightarrow 0$), and therefore correspond to the case shown in figure 4. The curves for $\beta_L > 0$ follow a similar course, but show asymmetric shapes due to non-linearities resulting from a finite flux contribution $\Phi_{\text{scr}} > 0$ of the screening current. This effect becomes particularly important for $\Phi_{\text{rf}} \rightarrow 0$, while the influence of β_L on the characteristics gets smaller when increasing

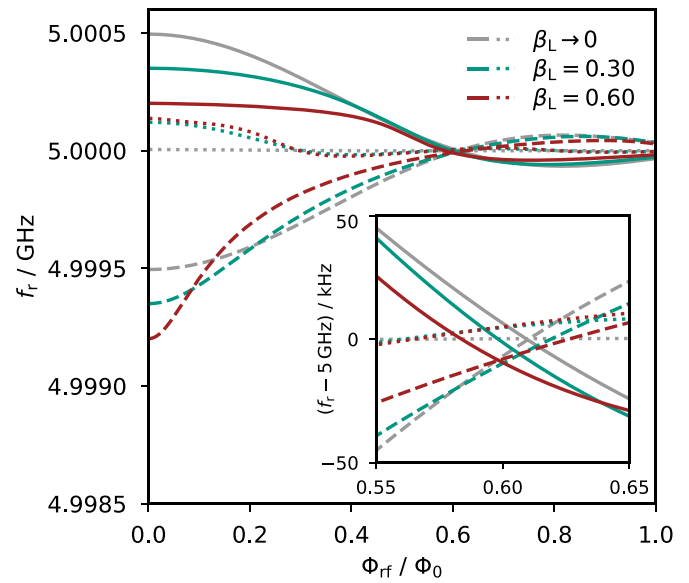


Figure 7. Dependence of the resonance frequency $f_r(\Phi_{\text{rf}})$ on the flux amplitude Φ_{rf} of the readout signal calculated by using our model being based on a 10th order Taylor expansion for different SQUID hysteresis parameters β_L . The values of the magnetic flux are $\Phi_{\text{ext}} = n\Phi_0$ (solid lines), $\Phi_{\text{ext}} = (n \pm 1/4)\Phi_0$ (dotted lines) and $\Phi_{\text{ext}} = (n + 1/2)\Phi_0$ (dashed lines). The ratio M_T^2/L_S for all curves is chosen such that the maximum resonance frequency shift $\Delta f_r^{\text{max}}(\varphi_{\text{rf}} \rightarrow 0) = 1$ MHz is identical for different values of β_L , whereas all other curve parameters correspond to the parameters chosen in figure 2.

the readout power. It should be noted that the curves do not intersect exactly at the first zero of the Bessel function $J_1(\varphi_{\text{rf}})$, as it is the case for $\beta_L \rightarrow 0$. However, as one can see in the inset graph, this effect is only very small.

Figure 8 shows another non-linear effect which is predicted by our model. Here, the resonance curves with minimum and maximum resonance frequency, i.e. for $\Phi_{\text{ext}} = n\Phi_0$ and $\Phi_{\text{ext}} = (n + 1/2)\Phi_0$, are plotted for $\Phi_{\text{rf}} \rightarrow 0$ and $\Phi_{\text{rf}} = 0.8\Phi_0$. As one can see, the maximum resonance frequency shift is much smaller for high readout powers, and the resonance curves swap their position, i.e. $f_r(n\Phi_0) < f_r((n + 1/2)\Phi_0)$. These effects are expected and in good agreement with the results presented in figure 7. However, the resonance curves do not get shifted as a whole, but rather become distorted and asymmetric. This asymmetry is a result of the frequency-dependent amplitude of the driving current in the resonator termination. The maximum amplitude I_T (see equation (6)) is only reached exactly on resonance. Hence, for $f \neq f_r$, the power in the resonator and therefore Φ_{rf} are always smaller than the maximum value. As a consequence, the power-dependent resonance shift is at maximum on resonance, whereas for $f \neq f_r$, the red lines for $\Phi_{\text{rf}} = 0.8\Phi_0$ tend to approach the corresponding green lines for $\Phi_{\text{rf}} \rightarrow 0$ instead of keeping their shape. Analytical expressions which describe these typical resonance curve asymmetries could not be derived within the context of this work, which is why the characteristics shown in figure 8 are calculated numerically, using an iterative method in combination with our analytical approximation model.

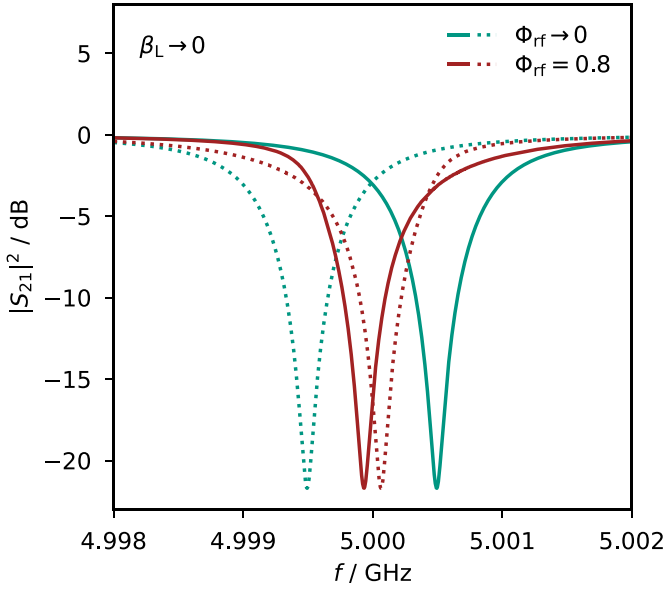


Figure 8. Frequency dependence of the transmission amplitude $|S_{21}(f)|^2$ in the low power limit and for high readout powers. The values of the magnetic flux are $\Phi_{\text{ext}} = n\Phi_0$ (solid lines) and $\Phi_{\text{ext}} = (n + 1/2)\Phi_0$ (dotted lines). All curves are numerically calculated, using our model and an iterative method. While the characteristics for very low readout power are identical to the curves shown in figure 2, the curves for high readout power are strongly asymmetric.

4. Comparison between our model and measured μ MUX characteristics

For verification of our μ MUX model, data from measurements described in [15] were used. Here, the scattering parameter $S_{21}(f, \Phi_{\text{ext}}, \Phi_{\text{rf}})$ of various channels of a μ MUX device for different values of the external flux Φ_{ext} and the amplitude Φ_{rf} of the driving signal were measured using a vector network analyzer (VNA). While the external flux Φ_{ext} was varied by changing the current I_{mod} through the modulation coil of the μ MUX normally used for flux ramp modulation, the amplitude Φ_{rf} of the probing signal was varied by changing the VNA signal power P_{VNA} and hence the resonator readout power P_{rf} . For extracting the relevant resonator parameters from measured raw data, we applied the algorithm described in [16].

Figure 9 shows the transmission amplitude $|S_{21}(f)|^2$ of an arbitrary μ MUX channel for $\Phi_{\text{ext}} = n\Phi_0$ and $\Phi_{\text{ext}} = (n + 1/2)\Phi_0$. The measurement indicated by green color was performed at small readout power, i.e. $P_{\text{rf}} \rightarrow 0$. As expected by our model, both resonance curves have a symmetric shape and the resonance frequency is at maximum for $\Phi_{\text{ext}} = n\Phi_0$ and at minimum for $\Phi_{\text{ext}} = (n + 1/2)\Phi_0$. In contrast, the resonance curves recorded at $P_{\text{VNA}} = -15$ dBm switched their position, i.e. $f_r(\Phi_{\text{ext}} = n\Phi_0) < f_r(\Phi_{\text{ext}} = [n + 1/2]\Phi_0)$, and become asymmetric, both in full agreement with our model. However, in contrast to our model, the curves show different depths which depend on the actual value Φ_{ext} of the external flux. This results from the magnetic flux dependence

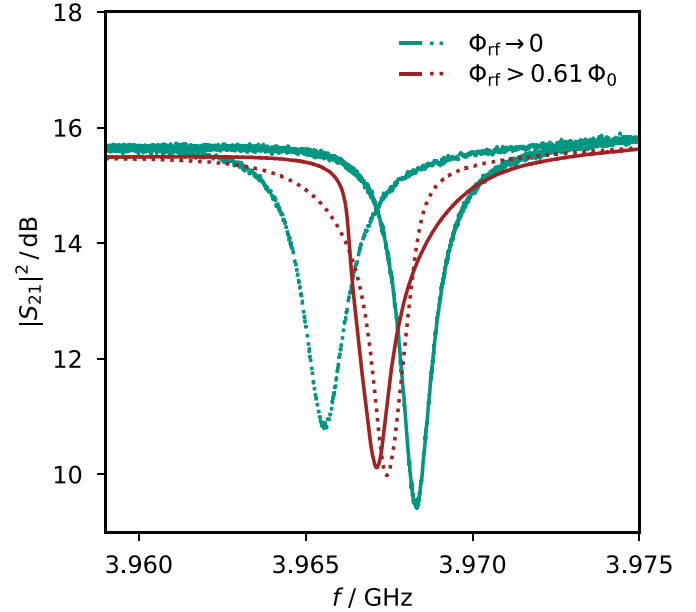


Figure 9. Measured transmission amplitude $|S_{21}(f)|^2$ for two different high frequency flux amplitudes Φ_{rf} . The values of the magnetic flux are $\Phi_{\text{ext}} = n\Phi_0$ (solid lines) and $\Phi_{\text{ext}} = (n + 1/2)\Phi_0$ (dotted lines). While the resonance curves for a negligibly small amplitude Φ_{rf} have a symmetric shape, the curves recorded at high resonator readout power P_{rf} show large asymmetries. In addition, the resonance frequencies of both flux states Φ_{ext} start to switch their position as expected by the prediction of the power-dependent μ MUX model.

of the internal quality factor $Q_i(\Phi_{\text{ext}})$ of the μ MUX channel as discussed in detail in [15]. This effect is not included in the model presented here as we are focusing solely on the dependence of the resonance frequency on readout power and SQUID hysteresis parameter.

For analyzing the dependence of the resonance frequency on the applied external flux Φ_{ext} , a current I_{mod} was sent through the common modulation coil of the μ MUX, generating a flux contribution of $\Phi_{\text{ext}} = M_{\text{mod}}I_{\text{mod}} + \Phi_{\text{off}}$ threading the SQUID loop. Here, M_{mod} denotes the mutual inductance between modulation coil and rf-SQUID and Φ_{off} a random, constant flux offset in the SQUID loop. The injected current was varied from $I_{\text{mod}} = -60 \mu\text{A}$ to $I_{\text{mod}} = 60 \mu\text{A}$ in steps of $1 \mu\text{A}$ for different readout powers P_{rf} , leading to the three characteristics shown in figure 10. For the curve with lowest readout power, i.e. $P_{\text{rf}} \rightarrow 0$, the parameter $\Phi_{\text{rf}} \rightarrow 0$ was set to a fixed value. Afterwards, a numerical fit motivated by equation (20) and based on the expression

$$f_r(I_{\text{mod}}, \Phi_{\text{rf}}) = f_{r,\text{off}} + \Delta f_{r,\text{mod}} \frac{2\beta_L}{\varphi_{\text{rf}}} \sum_i p_i(I_{\text{mod}}, \Phi_{\text{rf}}) \quad (21)$$

was performed. Subsequently, after determining and fixing the values of the parameters $f_{r,\text{off}}$, $\Delta f_{r,\text{mod}}$, β_L , M_{mod} and Φ_{off} , the same fitting procedure was applied to the other curves where the only free fitting parameter was Φ_{rf} . As expected by our model, the maximum resonance frequency shift Δf_r^{max} is

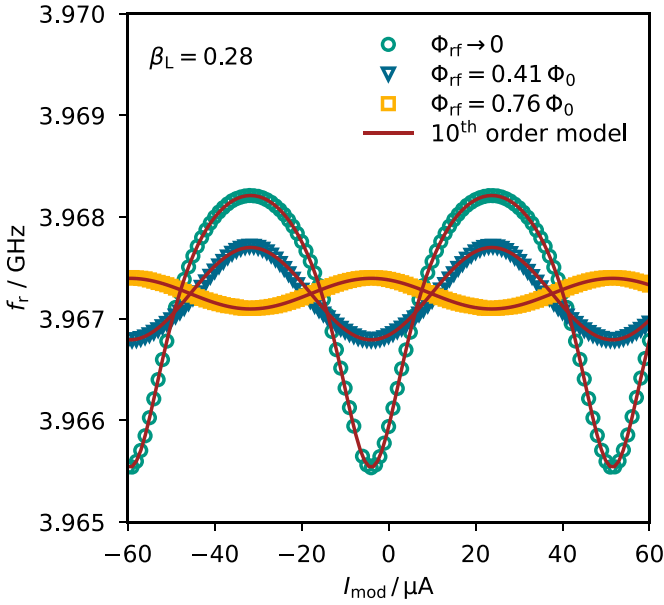


Figure 10. Measured resonance frequency $f_r(I_{\text{mod}})$ as a function of the modulation coil current I_{mod} for different high frequency flux amplitudes Φ_{rf} . In addition, for each curve a numerical fit is shown which is based on equation (21). While one curve was recorded at very low readout powers, i.e. $\Phi_{\text{rf}} \rightarrow 0$, the determined high frequency flux amplitude Φ_{rf} for the other curves is a result of the numerical fits.

largest for $\Phi_{\text{rf}} \rightarrow 0$ and decreases for higher applied readout signal amplitudes. Additionally, a sign change of the modulation can be observed solely for the curve with a high frequency flux amplitude of $\Phi_{\text{rf}} = 0.76 \Phi_0$, which is also in good agreement with our multiplexer model.

Figure 11 shows the dependence of the measured resonance frequency $f_r(P_{\text{VNA}})$ on the signal power P_{VNA} for different values of the external flux Φ_{ext} . Here, the modulation current I_{mod} was set to a fixed value to achieve the corresponding external flux Φ_{ext} , and the VNA readout power was varied from $P_{\text{VNA}} = -45$ dBm to $P_{\text{VNA}} = -15$ dBm in steps of 3 dBm. To convert VNA signal power P_{VNA} into readout power P_{rf} , an attenuation factor $A_{\text{rf}} < 1$ of the cryogenic microwave setup was introduced which is assumed to be independent of power and frequency, i.e. $P_{\text{rf}} = A_{\text{rf}} P_{\text{VNA}}$. This attenuation factor represents the attenuation of coaxial cables and high frequency components which are placed in between the VNA sending port and the μMUX chip on the cold stage of the cryostat. It is the only free parameter of the numerical fits, which are shown in the graph as well and which are based on equations (6) and (21). While the quality factors Q_i and Q_c in equation (6) are determined and fixed by means of the applied resonance curve analysis algorithm described in [16], all other μMUX parameters are set to the values given by the numerical fits shown in figure 10. At this point, the flux dependence of the internal quality factor $Q_i(\Phi_{\text{ext}})$ observed in figure 9 must be considered. As a result of different quality factors, the current $I_T(\Phi_{\text{ext}})$ in the resonator termination and therefore the generated high frequency flux amplitude $\Phi_{\text{rf}}(\Phi_{\text{ext}})$ are flux dependent as well. As a consequence, the numerical fit

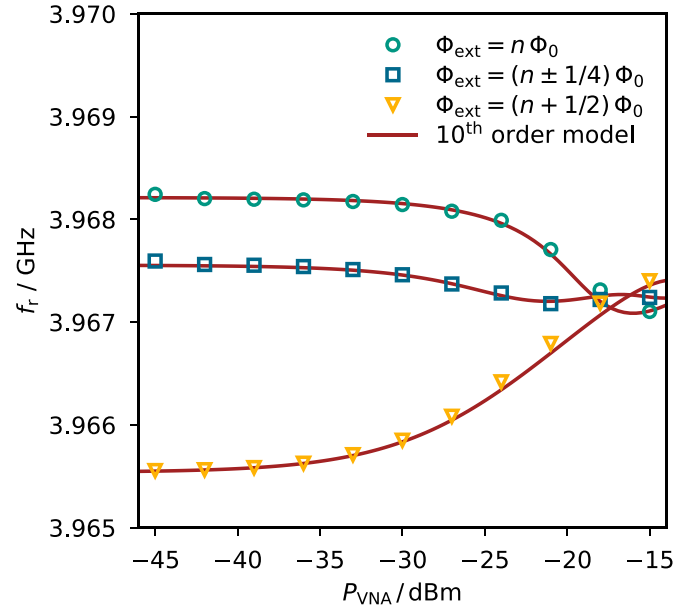


Figure 11. Measured resonance frequency $f_r(P_{\text{VNA}})$ as a function of the VNA signal power P_{VNA} for different values of the external flux Φ_{ext} . The numerical fits are based on equation (21) and contain only one free parameter which is the attenuation factor A_{rf} , that considers the total attenuation of the high frequency components between the VNA sending port and the μMUX chip. All other curve parameters are set to fixed values.

for $\Phi_{\text{ext}} = n \Phi_0$ with higher internal quality factor Q_i shifts toward lower VNA signal powers P_{VNA} , whereas the curve with $\Phi_{\text{ext}} = (n + 1/2) \Phi_0$ moves toward higher VNA signal powers P_{VNA} . As a result, the intersections of the three numerical fits in figure 11 are not as close together as shown in figure 7. Considering this effect, we yield a very good agreement between our model and experimental data.

5. Impact of our model

In the previous model, theoretical μMUX characteristics are given as a function of the total flux Φ_{tot} , whereas experimental data depend on the external flux Φ_{ext} . Therefore, a straightforward data analysis without using iterative numerical methods has only been possible for a negligibly small hysteresis parameter $\beta_L \rightarrow 0$ where $\Phi_{\text{tot}} \approx \Phi_{\text{ext}}$. Since most existing microwave SQUID multiplexers show hysteresis parameters in the range $0.2 \leq \beta_L \leq 0.6$, our model now allows for a direct comparison between theory and experiment as well as a prompt parameter extraction of measured μMUX devices for the first time.

In the context of μMUX optimization for a maximum signal-to-noise ratio, the previous model describes the HEMT noise contribution as a $\sqrt{S_{\Phi, \text{HEMT}}} \propto 1/P_{\text{rf}}$ dependence, proposing to choose a readout power P_{rf} as high as possible. However, when considering the decrease in the maximum resonance frequency shift Δf_r^{max} as shown in figures 4 and 7, it becomes clear that a specific value for the optimal readout power must exist. This has been recognized in the past, and different values have been suggested, e.g. readout powers

P_{rf} leading to a high frequency flux amplitude of $\Phi_{\text{rf}} \approx 0.16 \Phi_0$ [14] or $\Phi_{\text{rf}} \approx 0.3 \Phi_0$ [17]. With the help of our new model, we were able to set the optimum flux amplitude to $\Phi_{\text{rf}} \approx 0.3 \Phi_0$ for a wide μMUX parameter range respecting only theoretical considerations [18]. In addition to extracting the optimal μMUX readout power, our model also allows for the determination of the total attenuation of the transmitting cryogenic setup as it has been performed in figure 11, which replaces a cumbersome cryostat calibration measurement. Furthermore, our model allows for a precise, full numerical μMUX emulation including all known relevant effects and methods like finite resonator response time and flux ramp modulation. Due to the very accurate modeling including non-linear effects as shown in figure 8, our new model enabled us to increase the signal-to-noise ratio of μMUX devices by finding new, non-standard parameter sets [18].

Ultimately, our new model allows for the invention of new hybrid readout techniques that include principles of microwave SQUID multiplexing [19].

6. Conclusion

We presented an analytical model being able to describe the readout power dependence of the resonance frequency on the amplitude P_{rf} of the readout signal as well as the SQUID hysteresis parameter β_L . For this, we analyzed the Fourier components of the non-linear response of the non-hysteretic rf-SQUID. We were able to derive an analytical approximation describing the multiplexer in the parameter range of $\beta_L < 0.6$ and showed that our model includes the existing model as a limiting case. We verified our model by comparing it to measurements. Here, we demonstrated a very good agreement between measured multiplexer characteristics and model predictions. Our model hence allows for a deep understanding of the complex μMUX behavior, a prerequisite for a full device optimization as being required for realizing next-generation detector instruments strongly relying on the use of SQUID-based multiplexing techniques with high multiplexing factor.

Data availability statement

The data that support the findings of this study are available upon reasonable request from the authors.

Acknowledgments

This work was performed within the framework of the DFG research unit FOR 2202 (funding under Grant Nos. EN299/7-1, EN299/7-2, EN299/8-1, and EN299/8-2). The research leading to these results has also received funding from the European Union's Horizon 2020 Research and Innovation Programme, under Grant Agreement No. 824109.

ORCID iDs

M Wegner  <https://orcid.org/0000-0001-7747-2776>
S Kempf  <https://orcid.org/0000-0002-3303-128X>

References

- [1] Drung D, Assmann C, Beyer J, Kirste A, Peters M, Ruede F and Schurig T 2007 *IEEE Trans. Appl. Supercond.* **17** 699–704
- [2] Clarke J and Braginski A 2004 *The SQUID Handbook: Fundamentals and Technology of SQUIDs and SQUID Systems* vol 1 (Weinheim: Wiley)
- [3] Ullom J N and Bennett D A 2015 *Supercond. Sci. Technol.* **28** 084003
- [4] Kempf S, Fleischmann A, Gastaldo L and Enss C 2018 *J. Low Temp. Phys.* **193** 365–79
- [5] Ade P et al 2019 *J. Cosmol. Astropart. Phys.* **2019** 056
- [6] Alpert B et al 2015 *Eur. Phys. J. C* **75** 112
- [7] Gastaldo L et al 2017 *Eur. Phys. J. Spec. Top.* **226** 1623–94
- [8] Doriese W B et al 2016 *J. Low Temp. Phys.* **184** 389–95
- [9] den Hartog R H et al 2014 *J. Low Temp. Phys.* **176** 439–45
- [10] Mates J A B, Hilton G C, Irwin K D, Vale L R and Lehnert K W 2008 *Appl. Phys. Lett.* **92** 023514
- [11] Morgan K M et al 2016 *Appl. Phys. Lett.* **109** 112604
- [12] Reintsema C D et al 2008 *J. Low Temp. Phys.* **151** 927–33
- [13] Irwin K and Lehnert K 2004 *Appl. Phys. Lett.* **85** 2107–9
- [14] Mates J A B 2011 *The microwave SQUID multiplexer PhD Thesis* University of Colorado
- [15] Kempf S, Wegner M, Deeg L, Fleischmann A, Gastaldo L, Herrmann F, Richter D and Enss C 2017 *Supercond. Sci. Technol.* **30** 065002
- [16] Probst S, Song F B, Bushev P A, Ustinov A V and Weides M 2015 *Rev. Sci. Instrum.* **86** 024706
- [17] Mates J A B et al 2017 *Appl. Phys. Lett.* **111** 062601
- [18] Schuster C, Wegner M and Kempf S 2022 *J. Low Temp. Phys.* submitted
- [19] Schuster C, Wegner M, Enss C and Kempf S 2022 *Appl. Phys. Lett.* **120** 162601